

## LETTERS

# The dynamics of melt and shear localization in partially molten aggregates

Richard F. Katz<sup>1</sup>, Marc Spiegelman<sup>1,2</sup> & Benjamin Holtzman<sup>1</sup>

The volcanoes that lie along the Earth's tectonic boundaries are fed by melt generated in the mantle. How this melt is extracted and focused to the volcanoes, however, remains an unresolved question. Here we present new theoretical results with implications for melt focusing beneath mid-ocean ridges. By modelling laboratory experiments<sup>1,2</sup>, we test a formulation for magma dynamics and provide an explanation for localized bands of high-porosity and concentrated shear deformation observed in experiments. These bands emerge and persist at 15°–25° to the plane of shear. Past theoretical work on this system predicted the emergence of melt bands<sup>3,4</sup> but at an angle inconsistent with experiments. Our results suggest that the observed band angle results from a balance of porosity-weakening and strain-rate-weakening deformation mechanisms. Lower band angles are predicted for greater strain-rate weakening. From these lower band angles, we estimate the orientation of melt bands beneath mid-ocean ridges and show that they may enhance magma focusing toward the ridge axis.

Recent experiments<sup>1,2</sup> demonstrate that partially molten aggregates deformed in simple shear develop localized melt bands of high porosity and enhanced strain (Fig. 1a). These bands emerge at low angles (~20°) to the plane of shear for a range of strain rates and stresses, and persist at low angles even after large shear strains. This pattern-forming instability presents a rare opportunity to test theories of magma transport in the Earth's mantle<sup>5–8</sup>. Magma dynamics theories use continuum equations for conservation of mass, momentum and energy to describe a two-phase system of low-viscosity magma in a deformable, permeable solid matrix and should be applicable to the experiments. Past theoretical work<sup>3</sup> showed that a porosity-weakening viscous material<sup>9</sup> undergoing extension is unstable: tension across a weak, high-porosity region leads to low pressure that, in turn, causes convergence of melt flow into that region, raising its porosity and further weakening it. This instability has been predicted to occur at scales smaller than the compaction length<sup>3,4,10,11</sup>, which is the intrinsic length-scale in magma dynamics theory<sup>5</sup>.

Past theoretical work predicts that melt bands emerge perpendicular to the direction of the maximum rate of extensional strain. This prediction results from assuming that the matrix viscosity depends only on porosity and weakens with increasing melt fraction. For simple shear geometry, Spiegelman<sup>4</sup> showed that bands oriented at 45° to the shear plane will grow fastest, whereas melt bands with angles greater than 90° will decay (Supplementary Fig. S1). Here we demonstrate that a viscosity that includes both porosity and strain-rate-weakening mechanisms can reproduce the emergence and persistence of melt bands at about 20° to the direction of maximum shear (a difference of 25° from past predictions), as observed in experiments.

A power-law form for strain-rate weakening is a commonly

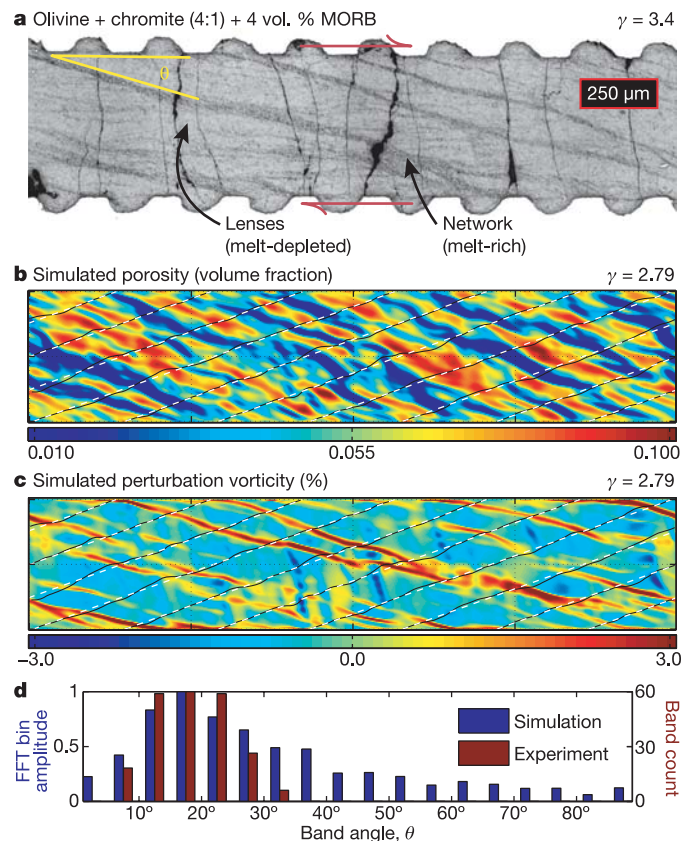


**Figure 1** | **A comparison of experimental and numerical results.** **a**, An example cross-section of an experiment (PI-1096) on a partially molten olivine–basalt–chromite aggregate deformed in simple shear to a strain of 3.4. (Adapted from Fig. 1a of ref. 18; experimental details in ref. 2.) The melt-rich bands are sloping, darker-grey regions at an angle  $\theta$  to the shear plane. Sub-vertical black features are decompression cracks, an experimental artefact. **b**, **c**, The porosity (**b**) and perturbation vorticity (**c**) from a numerical simulation with  $n = 6$  and  $\alpha = -27$  at a shear strain  $\gamma$  of 2.79. The domain is five by one compaction lengths, approximately equal to the estimated size of an experimental charge. The perturbation vorticity,  $\nabla \times [V - \gamma y i] / \dot{\gamma}$ , is the total vorticity minus the constant vorticity  $\dot{\gamma}$  due to simple shear (here normalized by  $\dot{\gamma}$ ). Black lines in **b** and **c** show the position of passive tracer particles that were arrayed in vertical lines at  $\gamma = 0$ ; white dotted lines show the expected position of the tracers due only to simple shear. The linear, low-angle red bands in **c** are weak regions associated with high porosity and enhanced shear, while the linear, sub-vertical blue regions are regions of reversed shear. **d**, Histograms comparing band-angle distributions in experiments and the numerical solution from **b**.

<sup>1</sup>Lamont-Doherty Earth Observatory of Columbia University, Palisades, New York 10964, USA. <sup>2</sup>Department of Applied Physics and Applied Mathematics, Columbia University, New York, New York 10027, USA.

accepted constitutive relation for high-temperature creep of mantle materials<sup>9,12</sup>. Here we assume<sup>9,12–14</sup>:

$$\eta(\phi, \dot{\epsilon}) = \eta_0 e^{\alpha(\phi - \phi_0)} \dot{\epsilon}_{II}^{\frac{1-n}{n}} \quad (1)$$

where  $\eta_0$  is the shear viscosity at the reference porosity  $\phi_0$  and reference strain rate.  $\alpha = -28 \pm 3$  is an experimentally derived porosity-weakening coefficient<sup>14,15</sup>,  $\dot{\epsilon}_{II}$  is the second invariant of the strain-rate tensor, and  $n$  defines the power-law dependence of viscosity on stress. This viscosity is newtonian when  $n = 1$  and is a standard non-newtonian power-law viscosity when  $n > 1$  and  $\phi = 0$ .

To understand the effect of the strain-rate dependence of viscosity we extend a previous linear analysis<sup>4</sup>. Formally, we introduce an infinitesimal plane-wave perturbation (analogous to a melt-rich band) to a constant-porosity system undergoing simple shear and solve for its growth as a function of orientation (Supplementary Information). The growth rate,  $\dot{s}$ , of porosity bands predicted by this analysis is:

$$\dot{s}(\theta, n) = -\frac{\alpha \xi (1 - \phi_0) \sin(2\theta)}{1 + \frac{1-n}{n} \cos^2(2\theta)} \quad (2)$$

where  $\theta(t)$  is the angle between the melt bands and the shear plane (Fig. 1a), which increases with time,  $t$ , due to advection by the shear flow. The parameter  $\xi = (\xi_0/\eta_0 + 4/3)^{-1}$  depends on the ratio of bulk viscosity to shear viscosity and controls the growth rate of band

porosity through the product  $\alpha \xi$ . The amplitude of porosity in the bands at strain  $\gamma(t)$  is given by  $e^{s(t)}$ .

Figure 2a shows the growth rate of melt bands as a function of their angle to the shear plane,  $\theta$ , and the stress exponent,  $n$ . For a viscosity that weakens with porosity only, melt bands oriented at 45° grow fastest because they are perpendicular to the direction of maximum extension in simple shear (equation (2) with  $n = 1$ ).

For a strain-rate-dependent viscosity ( $n > 1$ ), however, concentrated shear deformation further weakens the bands, allowing them to more easily de-compact under extension. Enhanced shear strain is largest for porosity bands oriented at zero and 90° and goes to zero for 45° bands (Supplementary Fig. S1 and  $\cos^2(2\theta)$  term in equation (2)). Thus two competing processes affect the preferred angle of melt bands. The balance between favourable orientation for extension (45°) and favourable orientation for concentrating shear (0 and 90°) is controlled by the factor  $(1 - n)/n$ . Figure 2a shows the effect of changing  $n$  on the growth rate of porosity. As  $n$  increases from 1 to 6, the single peak in  $\dot{s}$  at 45° broadens and divides into symmetric peaks at low (~15°) and high (~75°) angle.

Although the instantaneous growth rate of melt bands in Fig. 2a is symmetric about 45°, advection by simple shear affects low- and high-angle bands differently. Low-angle bands are rotated slowly and persist in favourable orientations for growth of porosity. High-angle bands, however, are rapidly rotated away from angles with positive growth rates. Figure 2b shows that after a strain of  $\gamma = 1$ , bands at low

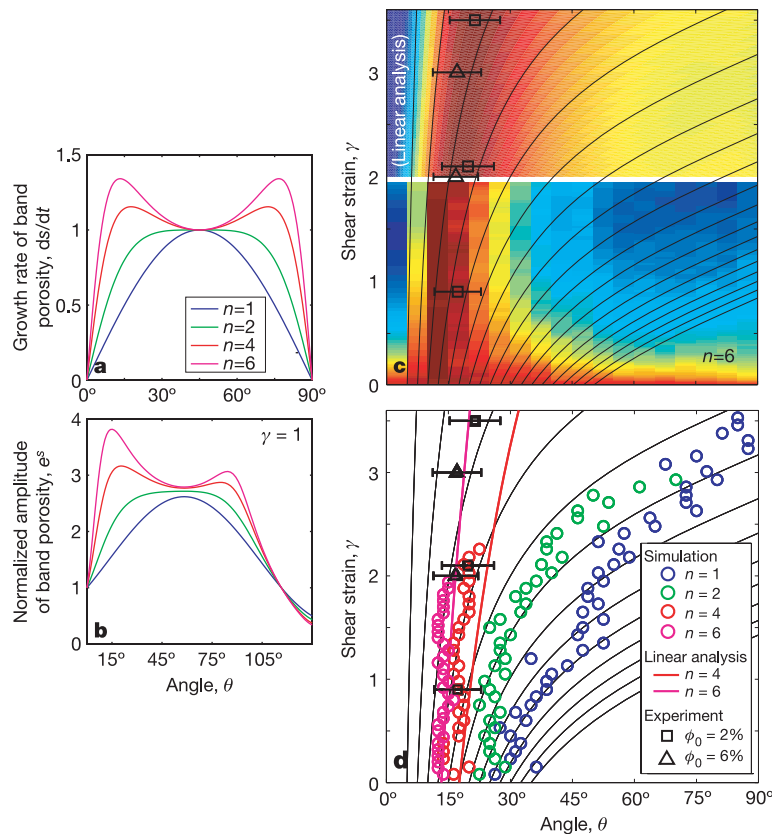


**Figure 2 | Results from linear analysis and numerical simulations, showing the effect of stress exponent  $n$  on the angular dependence of porosity of melt bands.** **a**, The growth rate  $\dot{s}$  of porosity as a function of angle; equation (2). **b**, The normalized amplitude of melt-band porosity as a function of  $\theta$  and  $n$  for  $\gamma = 1$ . Advection by simple shear preferentially rotates higher-angle bands out of favourable orientation for growth. The angle with peak amplitude at a given strain is determined by the growth rate and the rate of passive rotation by simple shear. **c**, Normalized, binned amplitude of FFTs of the porosity field from an ensemble of numerical simulations with  $n = 6$  ( $n = 1, 4$  shown in Supplementary Fig. S4). Linear analysis is used to extend simulation results to

$\gamma = 3.6$  (Supplementary Fig. S2 shows angle evolution from linear analysis only). The colour scale goes from zero to one. **d**, Summary of simulation ensemble results for  $n = 1, 2, 4$  and  $6$ . Coloured symbols represent the peak of the band-angle histogram and each is consistent with the angle estimated by visual inspection of the porosity field. Black symbols with 1-sigma error bars represent mean band angles in experiments, quantified by hand-measurement of sectioned experimental-run products. Black lines demonstrate the rotational effect of unperturbed simple shear on selected initial band angles (Supplementary equation S17). The behaviour of full nonlinear calculations for high strain at  $n > 3$  is still unclear.

angle have a larger amplitude than those at high angle. The systematics of band rotation are detailed in Supplementary equation S17.

The linear analysis suggests that increasing the contribution of strain-rate weakening favours the growth of low-angle melt bands. To validate these results and to explore the behaviour of the full non-linear system requires computational solutions, which we have performed using the Portable Extensible Toolkit for Scientific computation<sup>16,17</sup> (see Supplementary Information). The simulations are initiated at a constant porosity plus <1% random noise. Output from a representative run is shown in Fig. 1b and c.

Histograms of the distribution of band angles are calculated from simulations by taking the two-dimensional fast fourier transform (FFT) of the porosity field and integrating the amplitude response within 5° bins in band angle  $\theta$  (Fig. 1d). An ensemble of simulations is run, each with the same  $n$  but different initial noise, to produce a composite histogram at each time-step. Figure 2c shows the evolution of the band-angle distribution with increasing strain for  $n = 6$ . The peak of this histogram is initially  $\sim 15^\circ$  and persists at low angle with increasing strain. The evolution of the peak angle is also shown by magenta circles in Fig. 2d, which charts the peak angle for ensembles of simulations with different  $n$ . Consistent with the linear analysis, a more nonlinear viscosity (higher  $n$ ) results in a lower initial peak band angle.

In Fig. 2d, the angle corresponding to the peak of each of the histograms increases with strain for all  $n$ . Although the increase is due to the rotational effect of advection by simple shear, the rate of increase cannot be fully explained by this rotation. Black curves in Fig. 2c and d show the angle of material lines as they are advected by unperturbed simple shear flow. It is evident that the orientations of melt bands produced in simulations and linear analysis do not track with these trajectories. The trajectories that melt bands follow have a lower rate of increase in angle with strain than do the black curves. These trajectories result from an interplay of the growth of melt bands in favoured orientation and the rotation of bands out of this orientation by simple shear. An animation of calculations with  $n = 6$  (Supplementary movie M1) shows reconnection of porosity bands, maintaining the dominance of those at low angle. This reorganization is similar to the pumping mechanism proposed by Holtzman

*et al.*<sup>18</sup>, in which fluid flows from bands that have been rotated to higher angles to newly forming bands at lower angles.

Data from experiments are shown by black symbols in Fig. 2c and d and can be directly compared to model results. These data show that the peak band angle is roughly constant at  $15\text{--}20^\circ$  to large strain. Up to  $\gamma \approx 2$ , the data are consistent with simulations with  $n = 4$  or 6. Our current numerical techniques have not been able to take these simulations to higher strain (see Supplementary Information). Linear analysis, which tends to give higher peak band angles at a given strain than do simulations (see Fig. 2d), can be used to extend band-angle evolution to higher strain than that achieved in simulations (Fig. 2c). In this case, the results for  $n = 6$  are most consistent with the data. However, nonlinear effects in numerical simulations such as band reconnection and realignment might lead to a lower peak band angle at a given  $n$ .

The general agreement between our calculations and experimental results helps to validate magma dynamics theory. In particular, both theory and experiment exhibit the emergence of low-angle melt bands on length scales shorter than the compaction length that persist at low angle and concentrate shear strain. This agreement demonstrates the importance of non-newtonian rheology for modelling deforming, partially molten aggregates. In detail, there are differences between experiments and theory. For example, bands produced in simulations have a smaller aspect ratio and edges that are less sharp than those in experiments. These differences may result from the specific form of the flow law that we have used. More work is needed to explore models that use other non-newtonian rheologies and other formulations of magma dynamics<sup>8</sup>. Nevertheless, both experiments and theory suggest that deformation-induced melt bands are a robust feature of partially molten aggregates.

These results have implications for magma transport in the mantle, for example beneath mid-ocean ridges. A fundamental observation of mid-ocean ridges is that the oceanic crust is formed within 10 km of the ridge axis, whereas melt production is believed to occur over a region extending about 100 km from the axis<sup>19</sup>. This implies some mechanism of melt focusing toward the axis. The melt-band-forming instability may contribute to melt focusing, in addition to other mechanisms that have been proposed<sup>20–22</sup>. To estimate the orientation of bands, we calculate the principal axes of the strain-rate tensor for flow beneath a mid-ocean ridge<sup>23</sup> (Fig. 3a). Red line segments are perpendicular to the axis of maximum extension rate and show the orientation of melt bands expected for a newtonian viscosity, which tend to point away from the ridge axis. However, experiments (and theory for non-newtonian viscosity) suggest that band orientation is rotated  $25^\circ$  from the red line segments and should be most pronounced in regions of high strain. With these assumptions, melt bands point towards the ridge axis (Fig. 3b). If melt bands form an interconnected, permeable network with this orientation, they would enhance focusing of melt<sup>24</sup>. To quantitatively test this conjecture requires large-scale magma dynamics simulations ( $\sim 100$  km) that include the effects of melt buoyancy and finite strain, with sufficiently fine spatial discretization to resolve features smaller than the compaction length ( $\sim 1\text{--}10$  km)<sup>5,13</sup>. Such calculations will be challenging but current results give confidence that simulations can be used to predict patterns of melt extraction from the mantle.

Received 2 January; accepted 30 June 2006.

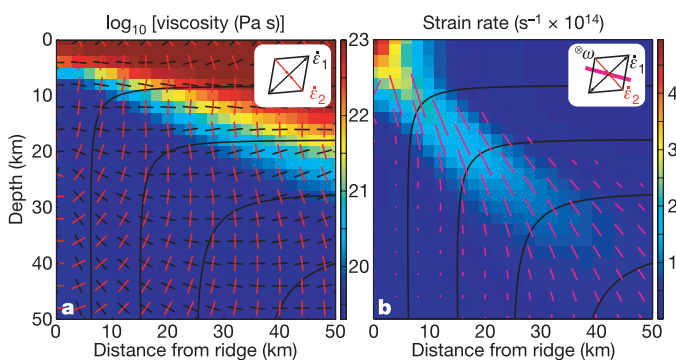


**Figure 3 | Estimated orientation of melt bands beneath a mid-ocean ridge from a two-dimensional, steady-state simulation of mantle flow<sup>23</sup>.** All fields have reflection symmetry about the line  $x = 0$ . **a**, Viscosity (colour), flow field (black streamlines), and principal axes of the strain-rate tensor for a temperature and strain-rate-dependent rheology. Red lines are perpendicular to the direction of maximum extension. For newtonian viscosity ( $n = 1$ ), red lines correspond to the orientation of melt bands in our model. Such bands would not focus melt toward the ridge axis. **b**, Strain rate (colour), flow field and melt-band orientation consistent with experiments (or in our model with  $n \approx 4\text{--}6$ ). Band orientations, indicated by magenta line segments, are calculated by rotating the red lines by  $25^\circ$  in the direction counter to the vorticity. The length of these segments is scaled to the local strain rate. If the bands form an interconnected permeable network, this orientation could help to focus melt to the ridge axis.

- Zimmerman, M., Zhang, S., Kohlstedt, D. & Karato, S. Melt distribution in mantle rocks deformed in shear. *Geophys. Res. Lett.* **26**, 1505–1508 (1999).
- Holtzman, B., Groebner, N., Zimmerman, M., Ginsberg, S. & Kohlstedt, D. Stress-driven melt segregation in partially molten rocks. *Geochem. Geophys. Geosyst.* **4**, 8607 (2003).
- Stevenson, D. Spontaneous small-scale melt segregation in partial melts undergoing deformation. *Geophys. Res. Lett.* **16**, 1067–1070 (1989).
- Spiegelman, M. Linear analysis of melt band formation by simple shear. *Geochem. Geophys. Geosyst.* **4**, 8615, doi:10.1029/2002GC000499 (2003).
- McKenzie, D. The generation and compaction of partially molten rock. *J. Petrol.* **25**, 713–765 (1984).

6. Scott, D. & Stevenson, D. Magma ascent by porous flow. *J. Geophys. Res.* **91**, 9283–9296 (1986).
7. Fowler, A. A mathematical model of magma transport in the asthenosphere. *Geophys. Astrophys. Fluid Dyn.* **33**, 63–96 (1985).
8. Bercovici, D., Ricard, Y. & Schubert, G. A two-phase model for compaction and damage 1. General theory. *J. Geophys. Res.* **106**, 8887–8906 (2001).
9. Hirth, G. & Kohlstedt, D. in *The Subduction Factory* (ed. Eiler, J.) 83–105 (AGU Geophysical Monograph 138, American Geophysical Union, Washington DC, 2003).
10. Richardson, C. Melt flow in a variable viscosity matrix. *Geophys. Res. Lett.* **25**, 1099–1102 (1998).
11. Hall, C. & Parmentier, E. Spontaneous melt localization in a deforming solid with viscosity variations due to water weakening. *Geophys. Res. Lett.* **27**, 9–12 (2000).
12. Karato, S. & Wu, P. Rheology of the upper mantle: A synthesis. *Science* **260**, 771–778 (1993).
13. Kelemen, P., Hirth, G., Shimizu, N., Spiegelman, M. & Dick, H. A review of melt migration processes in the adiabatically upwelling mantle beneath oceanic spreading ridges. *Phil. Trans. R. Soc. Lond. A* **355**, 283–318 (1997).
14. Mei, S., Bai, W., Hiraga, T. & Kohlstedt, D. Influence of melt on the creep behavior of olivine-basalt aggregates under hydrous conditions. *Earth Planet. Sci. Lett.* **201**, 491–507 (2002).
15. Kelemen, P., Shimizu, N. & Salters, V. Extraction of mid-ocean-ridge basalt from the upwelling mantle by focused flow of melt in dunite channels. *Nature* **375**, 747–753 (1995).
16. Knepley, M., Katz, R. & Smith, B. in *Numerical Solution of Partial Differential Equations on Parallel Computers* (eds Bruaset, A. & Tveito, A.) 413–438 (Lecture Notes in Computational Science and Engineering Vol. 51, Springer, Berlin, 2006).
17. Balay, S. *et al.* Portable Extensible Toolkit for Scientific computation (PETSc) (<http://www.mcs.anl.gov/petsc>) (2001).
18. Holtzman, B., Kohlstedt, D. & Morgan, J. P. Viscous energy dissipation and strain partitioning in partially molten rocks. *J. Petrol.* **46**, 2593–2613 (2005).
19. Forsyth, D. *et al.* Imaging the deep seismic structure beneath a mid-ocean ridge: the melt experiment. *Science* **280**, 1215–1218 (1998).
20. Spiegelman, M. & McKenzie, D. Simple 2-D models for melt extraction at mid-ocean ridges and island arcs. *Earth Planet. Sci. Lett.* **83**, 137–152 (1987).
21. Morgan, J. Melt migration beneath mid-ocean spreading centers. *Geophys. Res. Lett.* **14**, 1238–1241 (1987).
22. Sparks, D. & Parmentier, E. Melt extraction from the mantle beneath spreading centers. *Earth Planet. Sci. Lett.* **105**, 368–377 (1991).
23. Katz, R., Spiegelman, M. & Carbotte, S. Ridge migration, asthenospheric flow and the origin of magmatic segmentation in the global mid-ocean ridge system. *Geophys. Res. Lett.* **31**, L15605, doi:10.1029/2004GL020388 (2004).
24. Daines, M. & Kohlstedt, D. Influence of deformation on melt topology in peridotites. *J. Geophys. Res.* **102**, 10257–10271 (1997).

**Supplementary Information** is linked to the online version of the paper at [www.nature.com/nature](http://www.nature.com/nature).

**Acknowledgements** This work was supported by the Department of Energy Computational Science Graduate Fellowship Program of the Office of Science and National Nuclear Security Administration in the Department of Energy, and the NSF. We thank B. Smith, M. Knepley and the PETSc team at Argonne National Laboratory. We are also grateful to E. Coon, P. Kelemen and the solid Earth geodynamics group at LDEO for discussions. Comments by M. Jellinek helped to improve the manuscript.

**Author Information** Reprints and permissions information is available at [npg.nature.com/reprintsandpermissions](http://npg.nature.com/reprintsandpermissions). The authors declare no competing financial interests. Correspondence and requests for materials should be addressed to R.F.K. ([katz@ldeo.columbia.edu](mailto:katz@ldeo.columbia.edu)).